Mesoporous molybdenum nitride nanobelts as an anode with improved electrochemical properties in lithium ion batteries

CrossMark

Han-Chul Park [1], Kyung-Hoon Lee [1], Young-Woo Lee, Si-Jin Kim, Da-Mi Kim, Min-Cheol Kim, Kyung-Won Park[*]

Department of Chemical Engineering, Soongsil University, Seoul 156-743, Republic of Korea

HIGHLIGHTS

- Mesoporous Mo_2N nanobelts (NBs) are prepared via a template-free synthesis.
- The Mo_2N NBs exhibit a well-defined mesoporous structure.
- The Mo_2N NBs show a one-dimensional nanostructure.
- The meso-Mo_2N NBs exhibit improved intercalation properties of lithium ions.

ARTICLE INFO

ABSTRACT

The well-defined mesoporous nanostructure electrodes have been known to have improved lithium ion reaction properties such as the lithium ion insertion/desertion reaction, cyclability, and high rate performance. We prepared mesoporous molybdenum nitride nanobelts via a template-free synthesis as an anode for lithium-ion batteries. The as-prepared molybdenum nitride nanobelts (meso-Mo_2N NBs) exhibited face-centered cubic Mo_2N phase, well-defined mesoporous structure, and growth of [100] direction with 1-dimensional structure. The meso-Mo_2N NBs showed the improved electrochemical reaction properties of lithium ions such as high specific capacity and high rate cycling performance due to low transport resistance and high lithium ion diffusion coefficient.

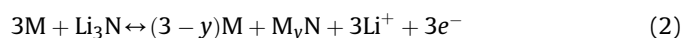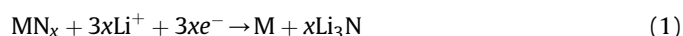© 2014 Elsevier B.V. All rights reserved.

1. Introduction

Lithium-ion batteries (LIBs) have been intensively attractive as energy storage devices because of their relatively high energy density and voltage than other energy storage devices, and room temperature operation. The LIBs consist of cathode materials including feature such as transition metal oxide containing lithium sources, anode materials including feature such as carbon, transition metal oxides and nitride, separator such as polyethylene, and electrolyte [1–4].

In particular, the electrode materials for LIBs are required high electrical conductivity and specific surface area, low cost, and long-term electrochemical stability [2–4]. Typically, for an anode in LIBs, the carbon-based materials have been used as promising electrode

materials, but show lower theoretical capacity in LIBs [5,6]. As an alternation electrode material, the ceramic materials such as transition metal oxide, nitride, and sulfide have been reported for electrode materials in LIBs. Among, the transition metal nitrides are well known as lithium ion insertion/desertion material with low production cost, non-toxicity, very low volume change during lithium ion insertion/desertion, good structural stability, high electrical conductivity, and long cycle life in LIBs [7–10].

In the LIBs, transition metal nitride is very intriguing anode materials. Generally, the well-known conversion reaction on transition metal nitrides is as follows:

$$MN_x + 3xLi^+ + 3xe^- \rightarrow M + xLi_3N \tag{1}$$

$$3M + Li_3N \leftrightarrow (3-y)M + M_yN + 3Li^+ + 3e^- \tag{2}$$

During first discharge reaction (Eq. (1)), the lithium ion is bonded with nitrogen of transition metal nitride (Li_3N) and the

* Corresponding author. Tel.: +82 2 820 0613; fax: +82 2 812 5378.
  E-mail addresses: kwpark@ssu.ac.kr, snow7292@naver.com (K.-W. Park).
[1] These authors contributed equally to this work.

separated transition metal atoms from transition metal nitride are transformed to metallic structure (M). On the other hands, the formed lithium nitride and metal during first discharge reaction regenerates transition metal nitride, which partially maintains lithium nitride in first charge reaction (Eq. (2)). In the subsequent cycles (Eq. (2)), the conversion reactions between lithium nitride and transition metal nitride have reversible reaction [11–17]. Thus, this can explain that the lithium ion insertion reaction of transition metal nitride is irreversible during first charge/discharge cycle, however, the second and subsequent cycles is reversible reaction and more stable.

However, the bulk structure of almost transition metal nitrides appears low specific capacity and electrochemical properties in LIBs because of a low specific surface area and an unfavorable diffusion distance of lithium in comparison with the structure-controlled nanoparticles [18]. To increase the lithium ion reaction properties, there have been many reports in the literature by structure and/or shape control of active materials, and mixed phase in active materials [19–21]. In particular, among them, the mesoporous nanostructures have major advantages such as many lithium ion reaction site and short diffusion distance of lithium ion for LIBs due to their highly specific surface area and controlled pore and channel in the nanometer range [22–24]. Unfortunately, the conventional template methods for synthesis of mesoporous materials are not simple because it is synthesized by template such as zeolite, mesoporous silica, and polymer [24,25].

In this work, the mesoporous molybdenum nitrides nanobelts with 1-dimensional structure were investigated as an anodic material for LIBs. Mesoporous nanostructure can be a candidate of high specific surface area with highly active site for LIBs electrodes. Furthermore, the belt-shaped nanostructures are expected to induce particular properties such as rapid electron collection of carriers and charge transport assisted by its 1-dimensional structure in LIBs electrodes. Accordingly, the main objective of this study is to investigate the lithium ion insertion/desertion reaction, cyclability, and high rate performance of the well-defined mesoporous molybdenum nitride nanobelts compared to that of irregular molybdenum nitride electrode in LIBs. Herein, we suggest the well-defined mesoporous molybdenum nitrides nanobelts with 1-dimensional structure as anode materials for LIBs. The well-defined mesoporous molybdenum nitrides nanobelts were synthesized by nitridation process using the molybdenum oxide nanobelts. The structural analysis of the as-prepared nanostructures was characterized using field-emission transmission electron microscopy (FE-TEM), field-emission scanning electron microscopy (FE-SEM), and X-ray diffraction (XRD). The specific surface area and pore size of the as-prepared electrodes were analyzed by a nitrogen sorption measurement. To evaluate the performance for LIBs, the charge–discharge and high rate curves, cyclic voltammograms (CVs), and electrochemical impedance spectroscopy of the electrodes were measured using lithium coin cells.

2. Experimental

2.1. Synthesis of mesoporous molybdenum nitride electrodes

For molybdenum oxide nanobelts (MoO_3) as a precursor, ammonium molybdate tetrahydrate (Sigma–Aldrich) was dissolved in 5 M HNO_3 with constant stirring at 25 °C for 1 h and then reacted in autoclave at 160 °C for 4 h. The resulting precipitate was washed several times with distilled water and dried in oven at 50 °C. The molybdenum oxide powder was heated at 700 °C for 6 h under the NH_3 flow of 100 mL min^{-1}. The product was cooled down to 25 °C in flowing NH_3, followed by passivation for 2 h in 100% air (denoted as meso-Mo_2N-NBs) [26]. For comparison, typical

molybdenum nitride nanoparticles (denoted as com-Mo_2N-NPs) were prepared by a nitrification process of commercial MoO_3 (Sigma–Aldrich) by means of heat treatment at 700 °C for 6 h under NH_3 atmosphere.

2.2. Structural characterization of as-prepared electrodes

The as-prepared samples were characterized by field-emission TEM using a Tecnai G2 F30 system operating at 300 kV. The TEM samples were prepared by placing a drop of the nanoparticle suspension in ethanol on a carbon-coated copper grid. SEM images were obtained on a JEOL JSM-6360A microscope operated 20 kV. Structural analysis of the samples was carried out by XRD method using a Bruker AXS D2 Phaser X-Ray Diffractometer with a Cu K_α radiation source of $\lambda = 0.15418$ nm with a Ni filter. Nitrogen adsorption and desorption isotherms were measured at 77 K using a Micromeritics ASAP 2020. Before the adsorption measurements, all samples were outgassed at 473 K for 360 min in the port of the adsorption analyzer. The starting relative pressure was 0.995 P/P_o and ending relative pressure was 0.01 P/P_o.

2.3. Electrochemical characterization of as-prepared electrodes

The electrodes were prepared by mixing 80 wt% Mo_2N nanostructure electrode as an active material, 10 wt% ketjen black as a conducting agent, and 10 wt% polyvinylidene fluoride (PVDF) as a binder. To obtain the slurry, several drops of N-methyl pyrrolidone were added into the mixture of Mo_2N powder with Ketjen black and PVDF. The mixed slurries were cast onto a Cu foil current collector and dried in air at 110 °C for 12 h. The electrode with an area of 1.32 cm^2 was dried at 70 °C vacuum oven. The electrodes were evaluated with respect to a lithium foil (FMC Corporation) counter electrode. The coin cells were assembled inside an Ar-filled glove box (<5 ppm, H_2O and O_2). The positive and negative electrodes of the cells were separated from one another by a porous polypropylene membrane (Wellcos) and an electrolyte solution consisting of 1.1 M $LiPF_6$ in ethylene carbonate:diethylcarbonate (1:1) solvent mixture (Techono Semichem). The electrochemical properties of the assembled cells were recorded with charge–discharge curves in a voltage window between 3.0 and 0.01 V vs. Li/Li$^+$. The charge–discharge tests were galvanostatically performed between 3.0 and 0.01 V vs. Li/Li$^+$ for 20 cycles at a current density of 100 mA g^{-1}. The charge–discharge tests were also performed at various current density from 100 to 4000 mA g^{-1} in order to evaluate the C-rate capability. For electrochemical impedance spectroscopic measurements, the excitation potential applied to the cells was 5 mV and the frequency ranged from 100 kHz to 10 mHz. All the electrochemical measurements were carried out at 25 °C. Furthermore, The CVs of the electrodes were obtained at 0.5 mV s^{-1} between 0 and 3 V vs. Li/Li$^+$ using a potentiostat (Eco Chemie, AUTOLAB).

3. Results and discussion

The meso-Mo_2N-NBs were prepared via template-free synthesis process, i.e. nitrification process of as-prepared molybdenum oxide nanobelts as a precursor at 700 °C under NH_3 atmosphere. Fig. 1(a) and (b) shows SEM image of MoO_3 nanoparticles as a precursor synthesized by hydrothermal method. The MoO_3 nanoparticles exhibit a belt type and single-crystalline orthorhombic structure grown into [110] direction (Fig. 1(c)–(f)). In particular, the FE-SEM and TEM images of the sample prepared using MoO_3 nanobelts are shown in Fig. 2. The as-prepared sample is a uniform mesoporous nanostructure with belt-type shape and pore diameter of ~4 nm (inset of Fig. 2(c)). The average length and width of the
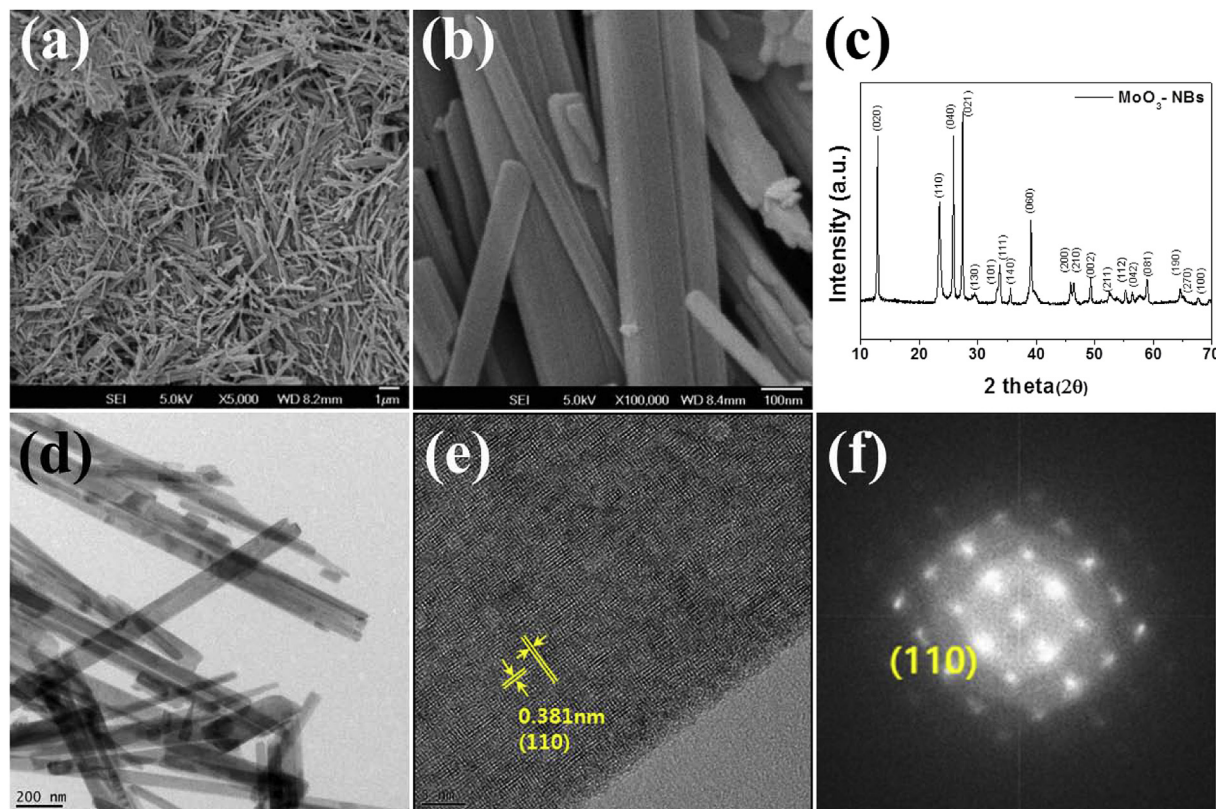
Fig. 1. (a) FE-SEM and (b) HR-SEM images of the molybdenum oxide nanobelts as a precursor. (c) XRD pattern of the molybdenum oxide nanobelts. (d) FE-TEM and (e) HR-TEM images of the molybdenum oxide nanobelts. (f) The fast Fourier-transform (FFT) pattern corresponding to the TEM image of (e).

meso-Mo_2N-NBs are ~3.5 μm and ~550 nm, respectively. The highly crystalline nature of meso-Mo_2N-NBs can be clearly observed in the HR-TEM image in Fig. 2(d), indicating one-directional growth into the [100] direction. The fringes with interplanar spacing of 2.09 Å correspond to (200) facet of the Mo_2N based on a face-centered cubic crystal structure. In particular, the inset of Fig. 2(d) shows the fast the Fourier transform (FFT) pattern of the meso-Mo_2N-NBs, which represents a single crystal of the Mo_2N phase and growth of [100] direction. In contrast, the com-Mo_2N-NPs synthesized by a nitrification process of commercial MoO_3 powder show an irregular size and shape with non-homogeneous pore distribution as shown in Fig. 3. The com-Mo_2N-NPs have interplanar spacing of 0.242 nm, that correspond to {111} facets of Mo_2N phase. This means that the belt-type shape and one-dimensional structure might be favorable for a template-free synthetic process of a uniform mesoporous structure.

In the XRD patterns of the as-prepared samples (Fig. 4), the diffraction peaks at 37.3°, 43.4°, 63.0°, 75.6°, and 79.6° correspond to (111), (200), (220), (311), and (222) planes, respectively, indicating that the resulting products hold a pure Mo_2N phase with unit cell parameter of 4.165 Å and space group of Pm-3m. In particular, the area ratio of (200) to (111) of meso-Mo_2N-NBs (0.947) is higher than com-Mo_2N-NPs (0.804). The diffraction peak from (200) plane for meso-Mo_2N-NBs is more intensified as compared to that of (200) for com-Mo_2N-NPs, suggesting that (200) plane for meso-Mo_2N-NBs is dominant, in good agreement with the HR-TEM result in Fig. 1(d).

To characterize surface area and pore size of the as-prepared Mo_2N samples, the Brunauer−Emmett−Teller (BET) curves were obtained using the com-Mo_2N-NPs and meso-Mo_2N-NBs as shown in Fig. 5. The com-Mo_2N-NPs exhibit an irregular pore structure and

low specific surface area of ~11.6 m^2 g^{-1} in comparison with the meso-Mo_2N-NBs (Fig. 5(a) and (b)). The hysteresis loop of com-Mo_2N-NPs is a type II curve that means a non-porous solid structure. The com-Mo_2N-NPs exhibit the separated adsorption/desorption region at 0.6 to 1.0 of relative pressure due to the formation of secondary pores through the gaps between particles. On the other hand, the hysteresis loop of meso-Mo_2N-NBs appears a type IV curve that means mesoporous structure [27]. The BET surface area and average pore size of the meso-Mo_2N-NBs are ~42 m^2 g^{-1} and ~4 nm, respectively (Fig. 5(c) and (d)). The surface area of the meso-Mo_2N-NBs is relatively higher compared to previous reports on Mo_2N [28].

In particular, the formation of the meso-Mo_2N-NBs might be related to atomic substitution, condensation, and belt-shape structure in nitrification process. As depicted in Fig. 6, the mesoporous molybdenum nitrides can be formed via a topotactic reaction using MoO_3 nanobelts in NH_3. The topotactic reaction is defined to occur when a solid product has well-defined crystallographical orientation relative to a starting material. During the present nitridation process, the increased oxygen vacancies in the molybdenum nitride might lead to the rearrangement of the oxide structure, producing a well-defined mesoporous structure by forming pores in the framework of the molybdenum nitride [18,29]. It is expected that the meso-Mo_2N-NBs having high specific surface area and well-defined pore can exhibit a high specific capacity for lithium ion insertion/desertion reaction and high rate performance compared to the com-Mo_2N-NPs.

Electrochemical properties of the samples were characterized using coin-type half cells with Li metal as an anode. Fig. 7(a) and (b) shows 1st charge−discharge curves of the com-Mo_2N-NPs and meso-Mo_2N-NBs at a current density of 100 mA g^{-1} between the
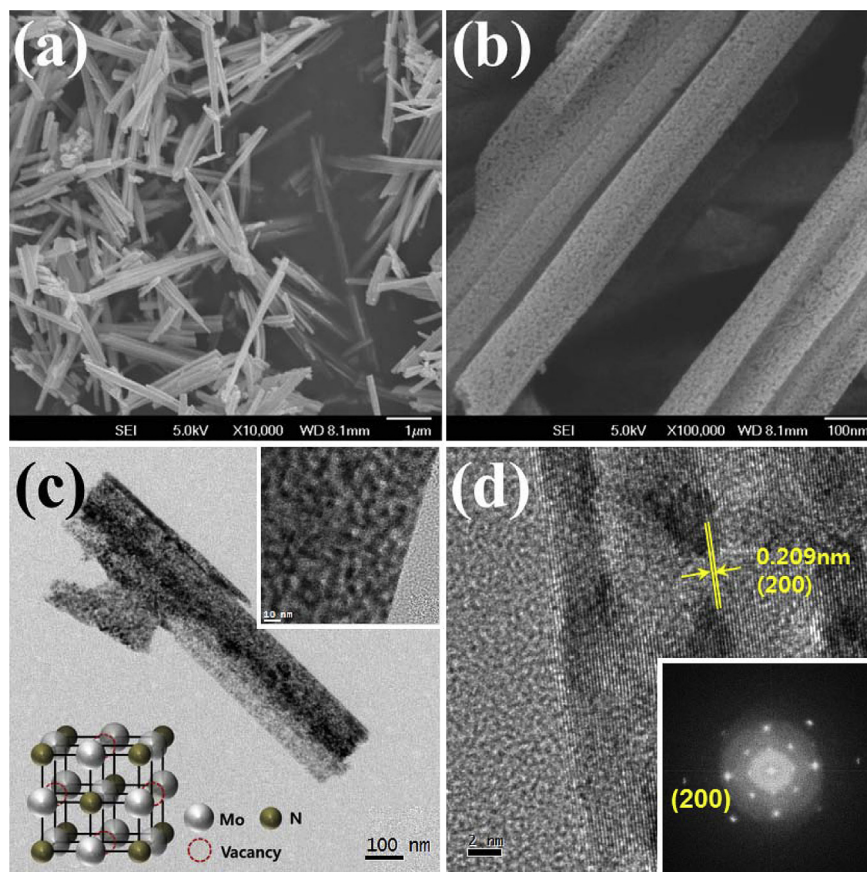
Fig. 2. (a) FE-SEM, (b) HR-SEM, (c) FE-TEM, and (d) HR-TEM images of meso-Mo_2N-NBs. The insets in (c) and (d) indicate HR-TEM image and the FFT pattern of meso-Mo_2N-NBs, respectively.
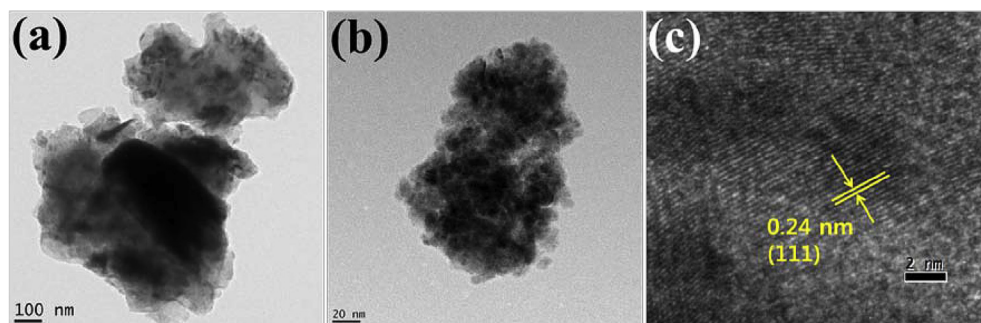

Fig. 3. FE-TEM ((a),(b)) and HR-TEM ((c)) images of com-Mo_2N-NPs synthesized by a nitrification process of commercial MoO_3.
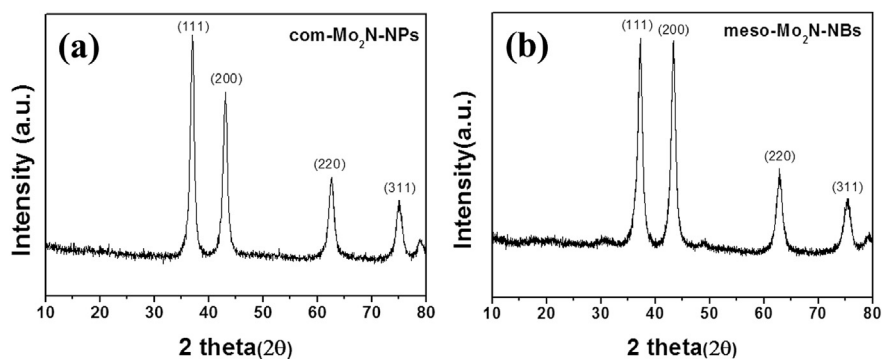

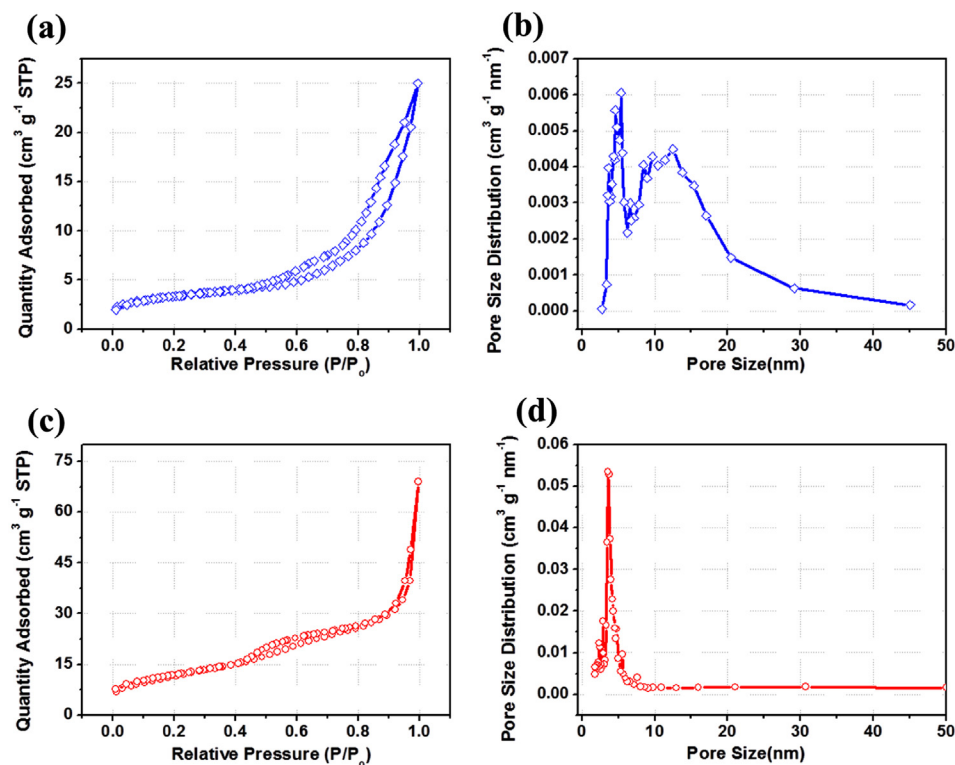**Fig. 4.** XRD patterns of (a) com-Mo_2N-NPs and (b) meso-Mo_2N-NBs.

Fig. 5. Nitrogen gas adsorption—desorption isotherms and pore size distributions of com-Mo_2N-NPs ((a),(b)) and meso-Mo_2N-NBs ((c),(d)).

voltage limits of 0.01—3.0 V vs. Li/Li$^+$, respectively. The 1st discharge capacities of the com-Mo_2N-NPs and meso-Mo_2N-NBs are 670 and 862 mAh g^{-1}, respectively. To investigate cycling performance and Coulombic efficiency of the electrodes, the discharge—charge curves were obtained at a constant current density of 100 mA g^{-1} for 20 cycles. As indicated in Fig. 8, the meso-Mo_2N-NBs display much improved cell performance with high reversible specific capacity and improved Coulombic efficiency in comparison with the com-Mo_2N-NPs. Furthermore, to evaluate and compare high rate performance of the electrodes, the discharge rate increased stepwise from 100 to 4000 mA g^{-1} as shown in Fig. 9(a) and (b). With increasing discharge rate, the specific discharge capacities of lithium ion of the meso-Mo_2N-NBs in all the range are

higher than those of the com-Mo_2N-NPs. The specific discharge capacity ratios of meso-Mo_2N-NBs to com-Mo_2N-NPs are 1.17 at 100 mA g^{-1}; 1.35 at 200 mA g^{-1}; 1.53 at 400 mA g^{-1}; 1.81 at 1000 mA g^{-1}; 2.26 at 2000 mA g^{-1}; 2.97 at 4000 mA g^{-1}. Especially, on the basis of the capacity at 100 mA g^{-1}, the relative reduction ratio of discharge capacity of the meso-Mo_2N-NBs at 4000 mA g^{-1} (50.9%) is much smaller than that of the com-Mo_2N-NPs (80.7%). The improved specific discharge capacity and high rate performance for the meso-Mo_2N-NBs might be mainly attributed to facilitating lithium ion insertion in the mesoporous belt-type nanostructure.

To identify electrochemical properties of the electrodes, CVs were obtained as shown in Fig. 10(a) and (b). In the 1st discharge
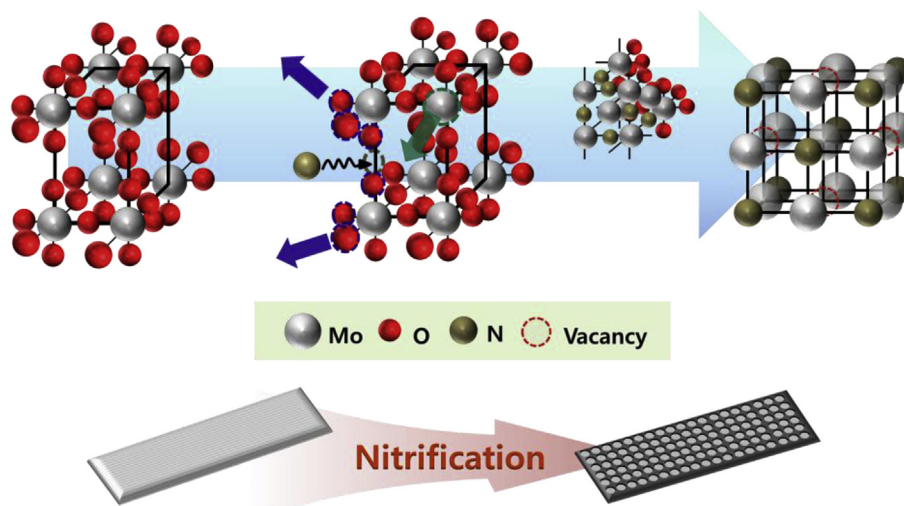

Fig. 6. Schematic illustration of meso-Mo_2N-NBs formed via a topotactic reaction using MoO_3 nanobelts as a precursor in NH_3 atmosphere.
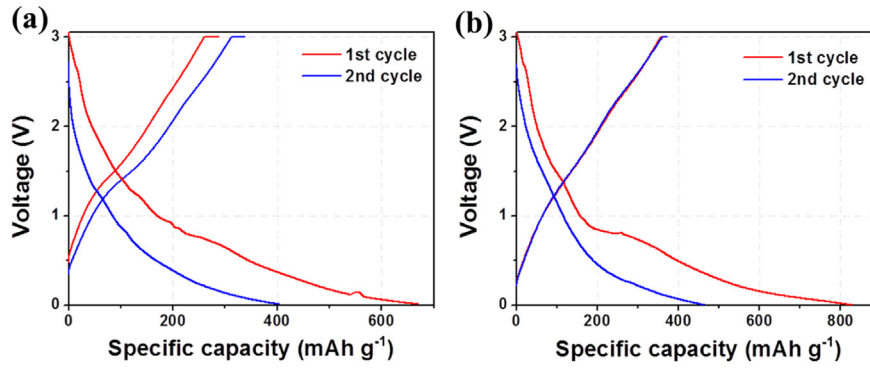
Fig. 7. Charge–discharge profiles of (a) com-Mo$_2$N-NPs and (b) meso-Mo$_2$N-NBs at a current density of 100 mA g^{-1} in the potential range of 0.01–3.0 V vs. Li/Li$^+$.
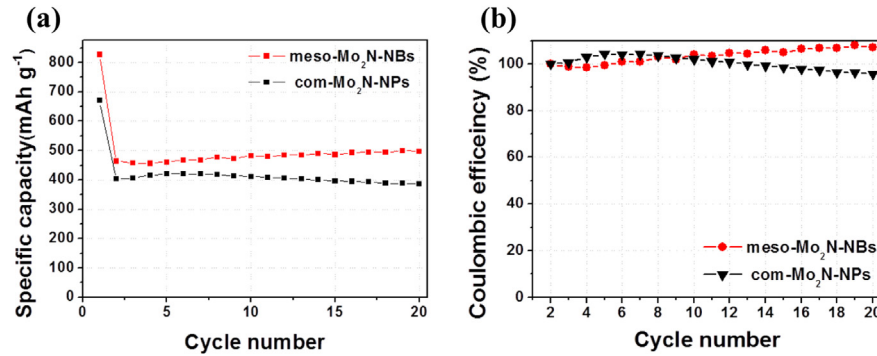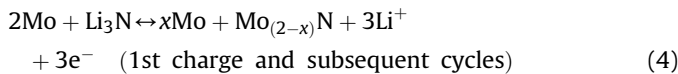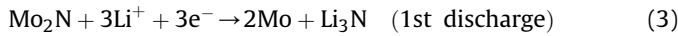

Fig. 8. (a) Specific discharge capacity and (b) Coulombic efficiency versus cycle number for the meso-Mo$_2$N-NBs and com-Mo$_2$N-NPs at a constant current density of 100 mA g^{-1}.

curves, the as-prepared electrodes exhibit irreversible reactions due to the formation of solid electrolyte interface layer and Li$_3$N phase (Eq. (3)) [13,15,30]. In the reaction of Eq. (4), electrons are mainly located on the metallic molybdenum, while Li-ions are inserted on Li$_3$N as an ionic conducting material, resulting in a charge separation [11–17,31]. The mechanism of lithium ion insertion and desertion in molybdenum nitrides can be suggested as follows:

$$Mo_2N + 3Li^+ + 3e^- \rightarrow 2Mo + Li_3N \quad \text{(1st discharge)} \qquad (3)$$

$$2Mo + Li_3N \leftrightarrow xMo + Mo_{(2-x)}N + 3Li^+$$
$$+ 3e^- \quad \text{(1st charge and subsequent cycles)} \qquad (4)$$

In the CVs for the as-prepared electrodes, the peaks corresponding to the oxidation of Mo to Mo$_2$N appear at ~1.5 V in the 1st and 2nd charge curves. The peaks at ~1.5 and ~2.5 V are attributed to reduction and oxidation of the Li$_3$N, respectively, according to Eq. (4) [12,15,31,32]. Fig. 10(c) shows Nyquist plots of meso-Mo$_2$N-NBs and com-Mo$_2$N-NPs between 100 kHz and 10 mHz. The value of the diameter of the semicircle on the Z$_{real}$ axis is related to the charge transfer resistance (R$_{ct}$). The values of R$_{ct}$ of meso-Mo$_2$N-NBs and com-Mo$_2$N-NPs are 85.62 and 165.21 Ω, respectively, representing much improved charge transport for the meso-Mo$_2$N-NBs. As indicated in Fig. 10(d), using the relationship between Z$_{Re}$ and square root of frequency ($\omega^{-1/2}$) in the low frequency range (Eq. (5)), the Warburg impedance coefficients (σ_W) of meso-Mo$_2$N-NBs and com-Mo$_2$N-NPs are determined to be 30.90 and 127.11 Ω cm^2 s$^{-1/2}$, respectively.

$$Z_{Re} = R_e + R_{ct} + \sigma_W \omega^{-1/2} \qquad (5)$$

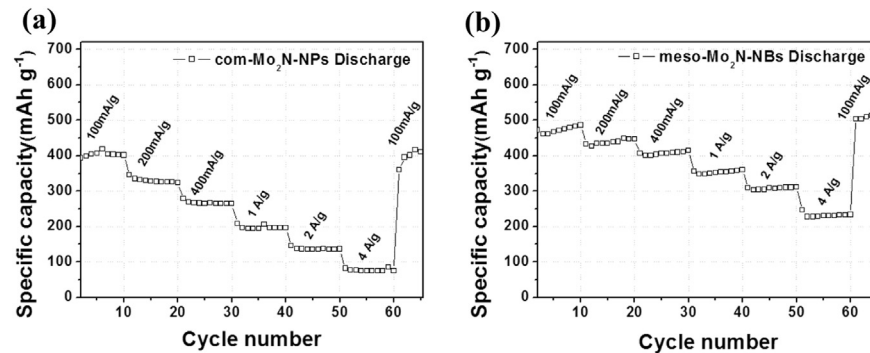$$D = R^2T^2 / 2A^2n^4F^4C^2\sigma_W^2 \qquad (6)$$

Fig. 9. Variation in discharge capacities versus cycle numbers for (a) com-Mo$_2$N-NPs and (b) meso-Mo$_2$N-NBs at different current rates between 0.01 and 3.0 V vs. Li/Li$^+$.
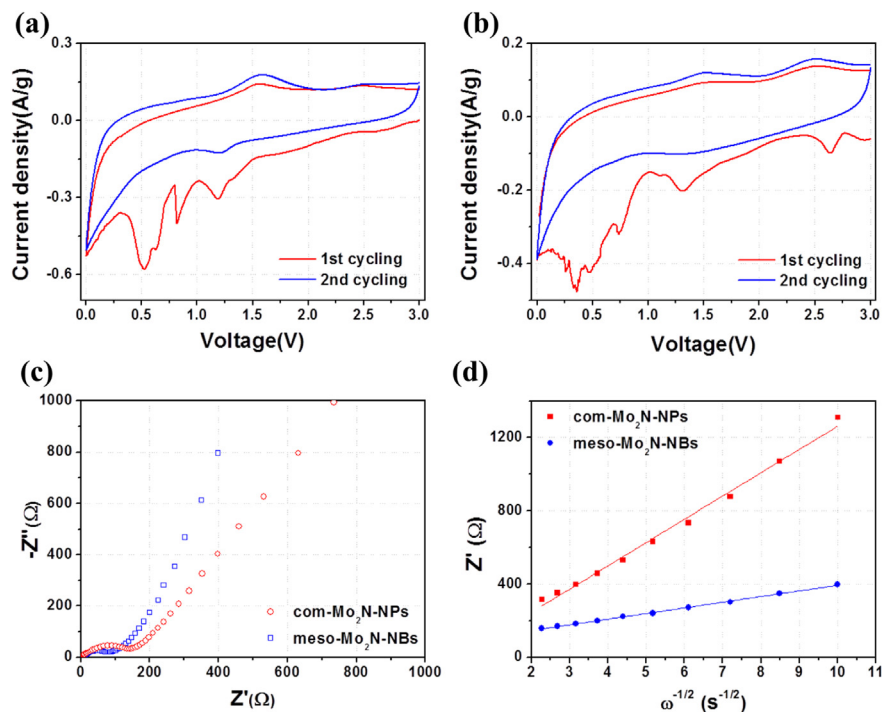
Fig. 10. CV plots of (a) com-Mo_2N-NPs and (b) meso-Mo_2N-NBs between 0 and 3.0 V versus Li/Li$^+$. (c) Nyquist plots of the samples in the frequency ranged between 100 kHz and 0.01 Hz. (d) Relationship between Z_{Re} and $\omega^{-1/2}$ in the low frequency range.

From the Eq. (6), the Li-ion diffusion coefficients of meso-Mo_2N-NBs and com-Mo_2N-NPs can be obtained to be 2.22×10^{-15} and 0.23×10^{-15} cm^2 s^{-1}, respectively, exhibiting much faster Li-ion diffusion process for the meso-Mo_2N-NBs. As a result, the improved lithium-ion reaction properties of the meso-Mo_2N-NBs, *i.e.* high specific capacity and excellent rate cycling performance may be attributed to low transport resistance, high diffusion coefficient, and short diffusion length of lithium ion in the mesoporous belt-type nanostructure electrode [33–35].

4. Conclusions

In summary, we demonstrated the mesoporous molybdenum nitride nanobelts with ~4 nm in an average pore size and ~42 m^2 g^{-1} in a specific surface area synthesized via a topotactic reaction by nitrification process under NH$_3$ atmosphere. The as-prepared meso-Mo_2N NBs showed a well-defined mesoporous belt-type nanostructure grown into [100] direction. The improved electrochemical reaction properties of lithium ion such as high specific capacity and excellent rate cycling performance in meso-Mo_2N NBs might be attributed to low transport resistance and high diffusion coefficient for lithium ions in comparison with the com-Mo_2N-NPs. Thus, by combining electrochemical data and structural analysis, it is concluded that the meso-Mo_2N NBs can be a promising anode candidate for LIBs.

Acknowledgments

References

[1] J.-M. Tarascon, M. Armand, Nature 414 (2001) 359–367.
[2] S. Lee, H.S. Kim, T.-Y. Seong, J. Alloy. Compd. 509 (2011) 3136–3140.
[3] H. Wang, D. Ma, X. Huang, Y. Huang, X. Zhang, Sci. Rep. 2 (2012) 701.
[4] S.-J. Kim, Y.-W. Lee, S.-B. Han, S.-B. Kim, W.-S. Kim, K.-W. Park, Int. J. Electrochem. Sci. 8 (2013) 3825–3833.
[5] H. Yue, F. Li, Z. Yang, J. Tang, X. Li, D. He, Mater. Lett. 120 (2014) 39–42.
[6] F. Cao, I.V. Barsukov, H.J. Bang, P. Zaleski, J. Prakash, J. Electrochem. Soc. 147 (2000) 3579–3583.
[7] Q. Sun, Z.-W. Fu, Electrochem. Solid-State Lett. 10 (2007) A189–A193.
[8] E. Panabière, N. Emery, S. Bach, J.-P. Pereira-Ramos, P. Willmann, Electrochim. Acta 97 (2013) 393–397.
[9] T. Song, K.C. Kil, Y. Jeon, S. Lee, W.C. Shin, B. Chung, K. Kwon, U. Paik, J. Power Sources 253 (2014) 282–286.
[10] M. Nishijima, N. Tadokoro, Y. Takeda, N. Imanishi, O. Yamamoto, J. Electrochem. Soc. 141 (1994) 2966–2971.
[11] F. Gillot, J. Oró-Solé, M.R. Palacín, J. Mater. Chem. 21 (2011) 9997–10002.
[12] P.P. Prosini, F. Cardellini, Electrochem. Commun. 4 (2002) 853–856.
[13] Z.-W. Fu, Y. Wang, X.-L. Yue, S.-L. Zhao, Q.-Z. Qin, J. Phys. Chem. B 108 (2004) 2236–2244.
[14] N. Pereira, M. Balasubramanian, L. Dupont, J. McBreen, L.C. Klein, G.G. Amatucci, J. Electrochem. Soc. 150 (2003) A1118–A1128.
[15] N. Pereira, L. Dupont, J.M. Tarascon, L.C. Klein, G.G. Amatucci, J. Electrochem. Soc. 150 (2003) A1273–A1280.
[16] L. Baggetto, N.A.M. Verhaegh, R.A.H. Niessen, F. Roozeboom, J.-C. Jumas, P.H.L. Notten, J. Electrochem. Soc. 157 (2010) A340–A347.
[17] N. Pereira, L.C. Klein, G.G. Amatucci, J. Electrochem. Soc. 149 (2002) A262–A271.
[18] C.H. Jaggers, J.N. Michaels, A.M. Stacy, Chem. Mater. 2 (1990) 150–157.
[19] B. Han, S.-J. Kim, B.-M. Hwang, S.-B. Kim, K.-W. Park, J. Power Sources 222 (2013) 225–229.
[20] S.H. Lee, S.-H. Yu, J.E. Lee, A. Jin, D.J. Lee, N. Lee, H. Jo, K. Shin, T.-Y. Ahn, Y.-W. Kim, H. Choe, Y.-E. Sung, T. Hyeon, Nano Lett. 13 (2013) 4249–4256.
[21] L.M. Reinold, M. Graczyk-Zajac, Y. Gao, G. Mera, R. Riedel, J. Power Sources 236 (2013) 224–229.
[22] M. Yang, M.J. MacLeod, F. Tessier, F.J. DiSalvo, J. Am. Ceram. Soc. 95 (2012) 3084–3089.
[23] W.A. Ang, Y.L. Cheah, C.L. Wong, R. Prasanth, H.H. Hng, S. Madhavi, J. Phys. Chem. C 117 (2013) 16316–21632.
[24] W. Li, Z. Wu, J. Wang, A.A. Elzatahry, D. Zhao, Chem. Mater. 26 (2014) 287–298.
[25] G.J.A.A. Soler-Illia, O. Azzaroni, Chem. Soc. Rev. 40 (2011) 1107–1150.
[26] K.-H. Lee, Y.-W. Lee, D.H. Kwak, J.-S. Moon, A.-R. Park, E.-T. Hwang, K.-W. Park, Mater. Lett. 124 (2014) 231–234.
[27] M. Thommes, Chem. Ing. Tech. 82 (2010) 1059–1073.
[28] J.-G. Choi, R.L. Curl, L.T. Thompson, J. Catal. 146 (1994) 218–227.
[29] N.S. Gajbhiye, R.S. Ningthoujam, Phys. Status Solidi C 1 (2004) 3449–3454.

[30] J. Liu, S. Tang, Y. Lu, G. Cai, S. Liang, W. Wang, X. Chen, Energy Environ. Sci. 6 (2013) 2691—2697.

[31] Q. Sun, Z.-W. Fu, Electrochim. Acta 54 (2008) 403—409.

[32] W. Ai, L. Xie, Z. Du, Z. Zeng, J. Liu, H. Zhang, Y. Huang, W. Huang, T. Yu, Sci. Rep. 3 (2013) 2341.

[33] J. Zhou, H. Song, B. Fu, B. Wu, X. Chen, J. Mater. Chem. 20 (2010) 2794—2800.

[34] B.-M. Hwang, S.-J. Kim, Y.-W. Lee, B. Han, S.-B. Kim, W.-S. Kim, K.-W. Park, Int. J. Electrochem. Sci. 8 (2013) 9449—9458.

[35] B. Pei, H. Yao, W. Zhang, Z. Yang, J. Power Sources 220 (2012) 317—323.